

# A nonlinear energy sink for tremor suppression using shape memory alloys

Abbas Jafarpour Mahalleh<sup>D</sup> and Mohammadreza Zakerzadeh

## Abstract

A passive vibration absorber is proposed to mitigate tremors induced by Parkinson's disease or essential tremor to replace costly and invasive alternatives. The proposed device is a wristband that, instead of classic spring-damper pairs, incorporates a shape memory alloy spring that acts as a nonlinear energy sink due to its hysteretic behavior. The mathematical models for the SMA spring and the patient's forearm and hand are developed. To demonstrate the superiority of the SMA absorber, the proposed absorber's performance is compared to a classic viscous absorber and also tested under unexpected harmonic forces. The simulations were performed in two parts. The first part used harmonic excitations as tremors to optimize SMA and viscous absorbers. The results indicated a 91% and 92% reduction in forearm and wrist tremors by the SMA absorber. The second part used real-world tremor data to compare the absorbers. Simulation results indicated that the viscous absorber reduces tremor power to an average of 55% in the 3–25 Hz range. In comparison, the SMA absorber has an average 92% tremor PSD reduction in the said range, which is significantly higher than the viscous absorber.

## Keywords

vibration absorber, Parkinson's disease, shape memory alloy spring, nonlinear energy sink, biomedical human hand model

## I. Introduction

Millions of people around the world are affected by tremors. This is characterized by involuntary movements of limbs (Deuschl et al., 1998), which can be caused by Parkinson's disease (PD), essential tremor (ET), or various drug misuses. The tremor generated from PD ranges between 3 and 5 Hz, whereas ET's tremor is more severe and ranges between 4 and 12 Hz (Louis, 1997). Unfortunately, as of now, neither PD nor ET are entirely curable. Therefore, when faced with these diseases, the primary focus is on mitigating symptoms to improve patients' life quality (Ruonala et al., 2014). Currently, pharmacotherapy is the most common treatment used to reduce tremors. However, it benefits roughly half of patients, while others experience severe side effects such as depression, confusion, and fatigue (Stoker et al., 2018). For drug-resistant patients, invasive procedures are advised but they can have side effects. To lower the risk of adverse effects, non-invasive methods such as biomedical loading can be used where a force is applied to the target limb to counter the tremor's movement. This loading is usually applied by wearable devices incorporating actuators (active) or energy-dissipating elements (semi-active or passive).

Passive wearable devices are the simplest and most cost efficient solutions for non-invasive hand tremor suppression. Fromme et al. (2020) developed a customizable

textile-based passive orthosis that can be inflated to reduce unintentional vibrations. When inflated, the air-filled structure gets bent or compressed by movement on the dorsal side of the wrist which counteracts unintentional tremor movements. The experimental results showed that the soft orthosis significantly reduced tremor power for ADL by 74 to 82%. Hosseini et al. (2020) studied the performance of the piezoelectric elements on mitigating tremor of the forearm. The device consisted of two piezoelectrics on the top and bottom of the forearm that acted as an actuator and a sensor, respectively. Results showed that the device could reduce the tremor amplitude in flexion-extension (FE) direction. Lu and Huang (2021) utilized particle dampers in an innovation to reduce the tremors. Their idea was derived from their previous work (Lu et al., 2012, 2017) where they developed particle dampers to reduce structural vibrations. Their experiments

---

School of Mechanical Engineering, College of Engineering, University of Tehran, Tehran, Iran

Received: 17 October 2023; accepted: 28 May 2024

### Corresponding author:

Mohammadreza Zakerzadeh, School of Mechanical Engineering, College of Engineering, University of Tehran, Tehran, Iran.  
 Email: [zakerzadeh@ut.ac.ir](mailto:zakerzadeh@ut.ac.ir)

indicated that the introduced particle damper has considerable effect on tremor reduction.

Despite the intensive use of passive systems for vibration reduction, these devices can only be effective in a narrow frequency range. If, over time, the tremor's frequency moves away from the absorber's effective range, a mistuning can happen, which will result in sub-optimal suppression or even tremor exacerbation (Alexander and Schilder, 2009). To counter this issue, nonlinear energy sinks (NESs) are proposed. In general, an NES is defined as an intrinsically nonlinear system that cannot be linearized (Ding and Chen, 2020). Specifically, NES systems can provide nonlinear restoring force, resulting in a wider effective frequency band (Wang et al., 2021). Further, it is known that NESs require less auxiliary mass than that of a linear vibration absorber (Gourdon and Lamarque, 2006), which can improve the patient's experience with the device. Taghipour and Dardel (2015) analyzed the responses of two NESs connected to a harmonically excited oscillator. They used a one DOF and a two DOF NES to reduce oscillator vibrations. They concluded that increasing the degree of freedom of the NES results in higher system robustness. Das et al. (2021) utilized shape memory alloy (SMA) springs in an NES with a negative stiffness for absorbing seismic vibrations.

In recent years, SMAs have been utilized in various use cases. Due to the existence of martensite and austenite in their microstructure and the constant interchange between them, these alloys exhibit high recoverability against large deformations under tensile loading (pseudoelasticity). The pseudoelasticity allows these alloys to dissipate energy through hysteretic behavior triggered by cyclic loading. This is why SMAs are used for passive vibration absorption as well (Lu et al., 2022). Shaw and Wang (2019) used two vibration absorbers consisting of SMA wires to reduce plate vibrations. They discovered that placing two perpendicular absorbers on a plate can cover six vibration modes. Park et al. (2021) proposed passive vibration reduction of a small satellite launch pad with superelastic SMA blades.

The main contribution of the current paper is utilizing shape memory alloy springs to build a cheap and low-maintenance vibration absorber to reduce tremors associated with PD or ET. Section 2 develops a mathematical relationship between the exerted force to a superelastic SMA spring and its end-to-end elongation. The design of the proposed wearable device is also introduced in this section (referred to as the SMA absorber). In Section 3, mathematical equations for a 3-DOF system consisting of the human forearm, wrist, and the absorber are derived. To demonstrate the superiority of the developed device, SMA springs are replaced with a classic spring-damper configuration (referred to as the viscous absorber) as

a benchmark. In Section 4, both SMA and viscous absorbers are optimized. Section 5 is divided into two parts. The first part presents the results of the optimization obtained by harmonic excitations. Later in the second part, both optimized absorbers are compared under real-world tremor data. Finally, the text ends with the Conclusion section.

## 2. Modeling of superelastic SMA spring

We used constitutive model obtained by Brinson (1993) to develop a relationship between the SMA spring's elongation and its reaction force. Brinson's model was initially developed for SMA wires under tensile loading, but inspired by the works of Liang and Rogers (1991) and Heidari et al. (2016), this model is generalized for shear loading. Originally, this model developed a relationship between temperature, strain, stress, and martensite ratio in a 1-dimensional SMA wire, as stated in (1).

$$\sigma - \sigma_0 = E(\varepsilon - \varepsilon_0) + \Omega(\xi - \xi_0) + \Theta(T - T_0) \quad (1)$$

where  $\sigma$ ,  $\varepsilon$ ,  $\Theta$ ,  $T$ ,  $E$ ,  $\Omega$ , and  $\xi$  represent stress, strain, thermal coefficient of expansion, temperature, Young's modulus, transformation tensor, and ratio of the martensite in the wire. The parameters with a 0 subscript represent the initial state of the specimen. Also, in this model, martensite ratio is the sum of stress ( $\xi_s$ ) and temperature ( $\xi_T$ )-induced martensite ratios, but because we have no temperature change, we can assume  $\xi = \xi_s$ . When the wire's temperature is above austenite finish temperature, deformations will change austenite in the wire microstructure to martensite. As long as the induced strain is smaller than the maximum recoverable strain ( $\varepsilon_L$ ), the deformation will recover (Mohd Jani et al., 2014). This effect is known as pseudoelasticity which is the backbone of the current study. The martensite ratio during phase transformation can be formulized as follows:

Austenite to martensite

$$\text{If } M_s < T \text{ and } \sigma_s^{cr} + C_M(T - M_s) < \sigma < \sigma_f^{cr} + C_M(T - M_s)$$

$$\begin{aligned} \xi_s = & \frac{1 - \xi_{s0}}{2} \cos \left\{ \frac{\pi}{\sigma_s^{cr} - \sigma_f^{cr}} \times [\sigma - \sigma_f^{cr} - C_M(T - M_s)] \right\} \\ & + \frac{1 + \xi_{s0}}{2} \end{aligned} \quad (2)$$

$$\xi_T = \xi_{T0} - \frac{\xi_{T0}}{1 - \xi_{s0}} (\xi_s - \xi_{s0}) \quad (3)$$

Martensite to austenite

$$\text{If } A_s < T \text{ and } C_A(T - A_f) < \sigma < C_A(T - A_s)$$

$$\xi = \frac{\xi_0}{2} \left\{ \cos \left[ a_A \left( T - A_s - \frac{\sigma}{C_A} \right) \right] + 1 \right\} \quad (4)$$

$$\xi_s = \xi_{s0} - \frac{\xi_{s0}}{\xi_0} (\xi_0 - \xi) \quad (5)$$

$$a_A = \frac{\pi}{A_f - A_s} \quad (6)$$

where  $C_M$  and  $C_A$  are constants that can be acquired from material's critical stress–temperature diagram, and  $A_f$ ,  $A_s$ , and  $M_s$  denote austenite start, austenite finish, and martensite start temperatures. Also,  $\sigma_s^{cr}$  and  $\sigma_f^{cr}$  are start and end of the alloy's critical stresses. The material properties of the SMA spring modeled in this work are adopted from the SMA-S1 in the research conducted by Huang et al. (2018).

To simplify (1), it is essential to note that there is negligible temperature change in pseudoelastic phase transformation. Also, the transformation matrix and Young's modulus ( $\Omega$  and  $E$ ) are both functions of the martensite ratio and can be written as follows:

$$\Omega(\xi) = -\varepsilon_L E(\xi) \quad (7)$$

Without loss of generality and assuming no temperature change, the initial state parameters can be considered zero at all times (Brinson and Huang, 1996). Thus (1) reduces to

$$\sigma = E(\xi) \times (\varepsilon - \varepsilon_L \xi) \quad (8)$$

The axial loading of the helical SMA spring leads to torsional and shear stress throughout its cross-section. As denoted by Heidari et al. (2016), Brinson's model can be generalized to shear loading by taking the shear strain as a composition of elastic shear strain ( $\gamma^e$ ) and shear strain induced by phase transformation ( $\gamma^{tr}$ ).

$$\gamma = \gamma^e + \gamma^{tr} \quad (9)$$

$$\begin{cases} \gamma^e = \frac{\tau}{G(\xi_s)} \\ \gamma^{tr} = \gamma_L \times \xi_s(\bar{\sigma}) \end{cases} \quad (10)$$

$$\tau = G(\xi_s)(\gamma - \gamma_L \times \xi_s(\bar{\sigma}, T)) \quad (11)$$

where  $\gamma$ ,  $\gamma_L$ , and  $\bar{\sigma}$  are, respectively, the shear strain, maximum recoverable shear strain, and effective tensile stress. Also  $G$  is the shear modulus of the specimen:

$$G(\xi) = \left( \frac{\xi}{G_M} + \frac{1-\xi}{G_A} \right)^{-1} \quad (12)$$

where  $G_M$  and  $G_A$  are the shear moduli of martensite and austenite, respectively. Using Von-Mises effective stress and strain, we can acquire effective stress and strain:

$$\bar{\sigma} = \sqrt{3}\tau \quad (13)$$

$$\bar{\varepsilon} = \frac{\gamma_L}{\sqrt{3}} \rightarrow \gamma_L = \sqrt{3} \times \varepsilon_L \quad (14)$$

It is important to note that SMA springs exhibit non-linear shear stress distribution in their cross-sections. Referring to Figure 1(a), as  $r$  increases, the shear stress increases in the cross-section which may result in austenite transforming to martensite. The spring's cross-section can be divided into three sections: (I) A linear-elastic region where the cross-section is full-austenite and stress is not enough for phase transformation ( $r \leq r_{Ts}$ ), (II) a nonlinear region where transformation takes place and  $\xi$  is non-zero ( $r_{Ts} \leq r \leq r_{Tf}$ ), and (III) a region where transformation is complete and the microstructure is entirely martensite ( $r_{Tf} \leq r \leq d/2$ ). It goes without saying that the existence of regions (II) and (III) relies on the amount of spring's loading. To reduce the computational cost of the analysis, as an engineering perspective, the martensite can be taken to be uniformly distributed throughout the cross-section with an approximate effective martensite ratio. Although this approach may be unrealistic, it has been employed by Enemark et al. (2014), Aguiar et al. (2010), and Mohammad Hashemi et al. (2019), and proved to be of reasonable accuracy.

Taking  $\xi$  to be homogeneous leads to a linear shear distribution in the cross-section of the spring. With this assumption, shear stress and strain in an arbitrary radii of  $r = a$  can be calculated as follows:

$$\tau_a = G(\bar{\xi}) \gamma_a \quad (15)$$

$$\gamma_a = \frac{a}{d} \gamma_{max} \quad (16)$$

where  $\gamma_{max}$  is the maximum shear strain at  $r = d/2$  and  $\bar{\xi}$  is the effective martensite ratio. The force equilibrium in spring's cross-section can be written as follows:

$$F = \frac{4\pi}{D} \int_0^{\frac{d}{2}} \tau r^2 dr \quad (17)$$

where D and d represent spring helix and coil diameters, respectively. Using (11) and (17) we have

$$\begin{aligned} F &= \frac{2\pi}{R} \int_0^r G(\bar{\xi}) \left( \frac{a}{r} \gamma_{max} - \gamma_L \bar{\xi} \right) a^2 da \\ &= \frac{2\pi r^3}{3R} G(\bar{\xi}) \left( \frac{3}{4} \gamma_{max} - \gamma_L \bar{\xi} \right) \end{aligned} \quad (18)$$

By comparing (18), (16), and (11) it can be inferred that the effective martensite ratio and strain can be calculated by taking  $r = \frac{3}{8}d$ . To establish a relationship between spring's restoring force and its elongation,  $\gamma_{max}$  needs to be acquired.

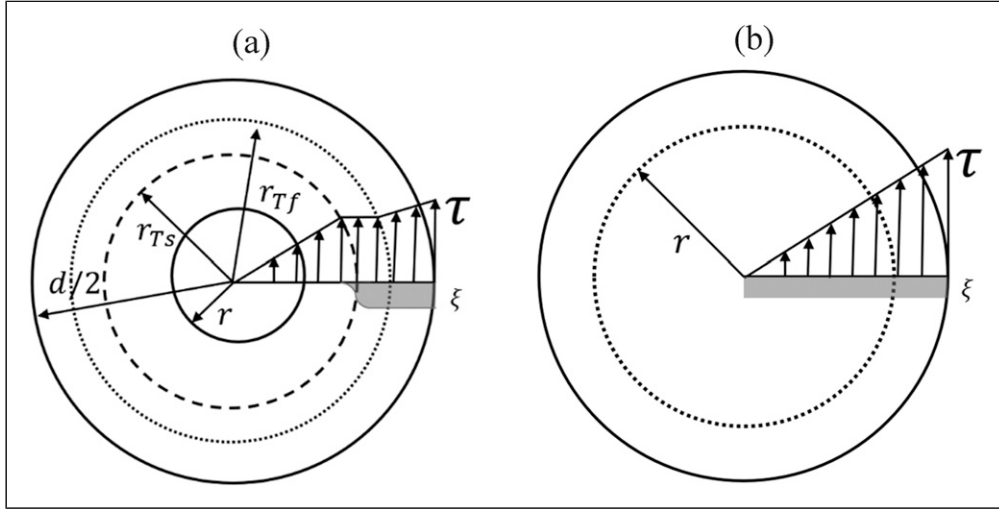


**Figure 1.** Shear stress distribution in helical SMA spring wire. The shear distribution is depicted as  $\tau$ , whereas the gray area denoted by  $\xi$  is the martensite ratio throughout the cross-section.  $d$  is the diameter of the spring wire. (a) SMA spring with non-linear shear and  $\xi$  distribution; (b) simplified SMA spring with linear shear and homogenous  $\xi$  distribution.

Referring to [Budynas and Nisbett \(2014\)](#), maximum shear stress and strain can be approximated:

$$\tau_{max} = \frac{8FD}{\pi d^3} \quad (19)$$

$$\gamma_{max} = \frac{\tau_{max}}{G} = \frac{8FD}{\pi d^3 G} \quad (20)$$

Also using Castiglione's theorem, spring's elongation can be calculated as follows:

$$\delta = \frac{8FD^3N}{d^4G} \left(1 + \frac{1}{2c^2}\right) \approx \frac{8FD^3N}{d^4G} \quad (21)$$

where  $\delta$  is the elongation and  $c = D/d$ . Using (20) and (21), maximum shear strain in cross-section can be related to spring's elongation.

$$\gamma_{max} = \frac{d}{\pi ND^2} \delta \quad (22)$$

Large deformations of the spring change its diameter which if not accounted for, may result in reduced accuracy of the model. Referring to [Whal \(1963\)](#), the refined spring's wire diameter is calculated in (23)–(26).

$$\alpha_0 = \tan^{-1}(L_0/(\pi ND_0)) \quad (23)$$

$$\alpha_1 = \sin^{-1} \left( \frac{\delta}{\mathcal{L}} + \sin(\alpha_0) \right) \quad (24)$$

$$\mathcal{L} = \frac{\pi ND_0}{\cos(\alpha_0)} = \frac{\pi ND_1}{\cos(\alpha_1)} \quad (25)$$

$$\frac{D_1}{D_0} = \frac{\cos(\alpha_1)}{\cos(\alpha_0)} \quad (26)$$

where  $\alpha$ ,  $L$ ,  $R$ ,  $D$ , and  $\mathcal{L}$  are, respectively, the spring's helix angle, length, radii, diameter, and the length of the wire that spring has been made of. The 0 subscripts denote the initial state of the spring while subscripts denoting 1 refer to the stretched spring. The validity of the obtained model is demonstrated in [Figure 2](#) where the simulation results are compared to the experiments conducted by [Huang et al. \(2018\)](#).

### 3. Dynamic model of the system

Tremor propagates because of limb and joint mechanics. It is possible to reduce all types of tremors to recurring torques driving movements in the patient's joints ([Davidson and Charles, 2017](#)). Therefore, a dynamic model of the human forearm and wrist is developed to model tremor propagation across patients' upper limbs. [Davidson and Charles \(2017\)](#) developed a 7-DOF model for analyzing tremor propagation from shoulder to wrist. [Kodek and Munih \(2003\)](#) and [Gebai et al. \(2018\)](#) modeled the shoulder, forearm, and hand of the patients as three connected rigid links that exhibit planar motion. [Ture Savadkoohi et al. \(2021\)](#), [Rahnavard et al. \(2014\)](#), and [Zubair et al. \(2022\)](#) used a 2-DOF planar model as a human hand and forearm system, where the shoulder and elbow were modeled as simple joints. Also in these models, the hand was taken as a concentrated mass connected to the tip of the forearm or its effective mass was added to the forearm's mass. In this paper, we have

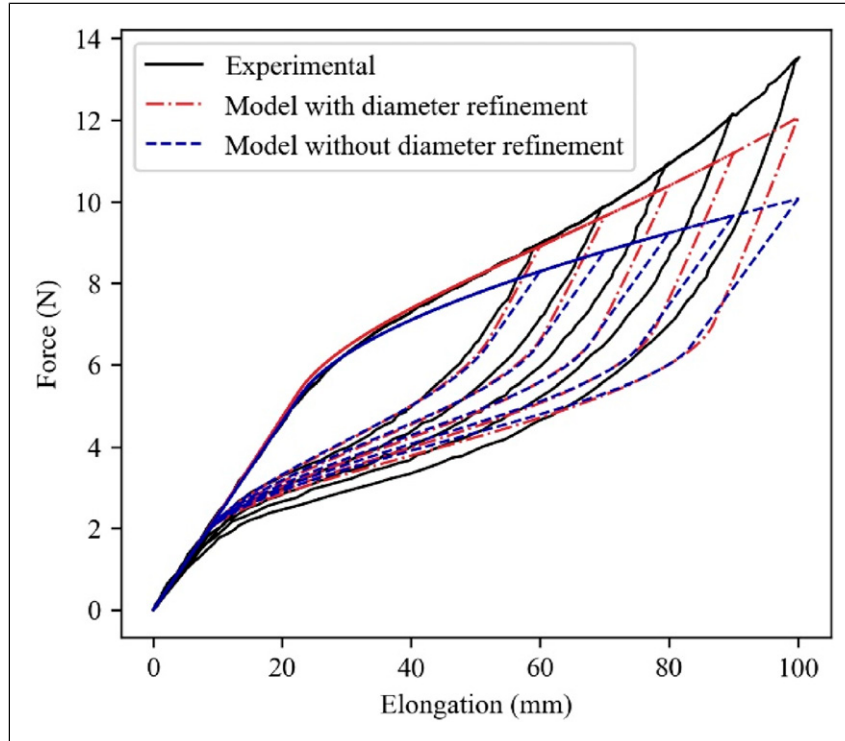


**Figure 2.** Validating the developed model with experimental results obtained by Huang et al. (2018) (case I): comparison between experimental data and simulation results with and without accounting for spring diameter change.

used a planar 3-DOF system to analyze the tremor response of the developed absorber.

The analyzed model is depicted in Figure 3, where the forearm and hand are modeled as two rigid bars with concentrated masses at *A* and *C*.  $\theta_1$  and  $\theta_2$  are the rotation angles of elbow and wrist joints in the FE direction. Also, the absorber is connected to the elbow at *D*.  $m_1$ ,  $m_2$ , and  $m_d$  are the concentrated masses of forearm, hand, and the absorber at their respective center of masses. Also  $x_d$  is  $m_d$ 's movement direction which is perpendicular to elbow at all times. Passive stiffness and damping of the joints are modeled as two rotational spring-dampers which are shown as spirals located at joints *O* and *B*. Figure 4 depicts a real-world representation of the suggested absorber placed on the patient's wrist. It consisted of two rings connected with

$$\vec{v}_A = \vec{v}_o + \vec{\omega} \times \vec{l}_{c1} = \dot{\theta}_1 l_{c1} \vec{J} \quad (27)$$

$$\begin{aligned} \vec{v}_{\text{absorber}} &= \vec{v}_D + \vec{\omega} \times \vec{x}_d + \vec{v}_{\text{rel}} \\ &= -\dot{\theta}_1 x_d \vec{I} + (-l_d \dot{\theta}_1 + \dot{x}_d) \vec{J} \end{aligned} \quad (28)$$

$$v_B = \dot{\theta}_1 \vec{K} \times l_1 \vec{I} = -l_1 \dot{\theta}_1 \vec{J} \quad (29)$$

where  $(\vec{I}, \vec{J}, \vec{K})$ ,  $(\vec{I}_B, \vec{J}_B, \vec{K}_B)$ ,  $l_1$ ,  $l_d$ ,  $l_{c1}$  and  $l_{c2}$  are unit vectors of the frames connected to elbow and wrist joints, forearm length ( $\overrightarrow{OB}$ ), distance of absorber from elbow joint ( $\overrightarrow{OD}$ ), distance of forearm and hand's center of mass from elbow ( $\overrightarrow{OA}$ ) and wrist ( $\overrightarrow{BC}$ ) joints, respectively.

$$\begin{aligned} \vec{v}_C &= \vec{v}_B + \vec{\omega} \times \vec{l}_{c2} + \vec{v}_{\text{rel}} = -l_1 \dot{\theta}_1 \vec{J} - (\dot{\theta}_1 + \dot{\theta}_2) l_{c2} \vec{I}_B \\ &= (-(\dot{\theta}_1 + \dot{\theta}_2) l_{c2} - l_1 \dot{\theta}_1 \sin(\theta_2)) \vec{I}_B + (-l_1 \dot{\theta}_1 \cos(\theta_2)) \vec{J}_B \end{aligned} \quad (30)$$

two coincident SMA springs. The outer ring is heavier than the inner ring while inner ring helps the absorber stay on the forearm.

The system's kinematics are determined using relative motion by taking three rotating frames at points *O*, *D*, and *B* (Figure 3).

The Lagrangian method has been used to develop the system's governing equations.

where  $T$ ,  $U$ ,  $Q$ ,  $q$ , and  $\mathfrak{R}$  are the kinetic energy, potential energy, generalized torques and forces, generalized coordinates, and Rayleigh dissipation factor of the system, respectively.

The kinetic energy of system is calculated as follows:

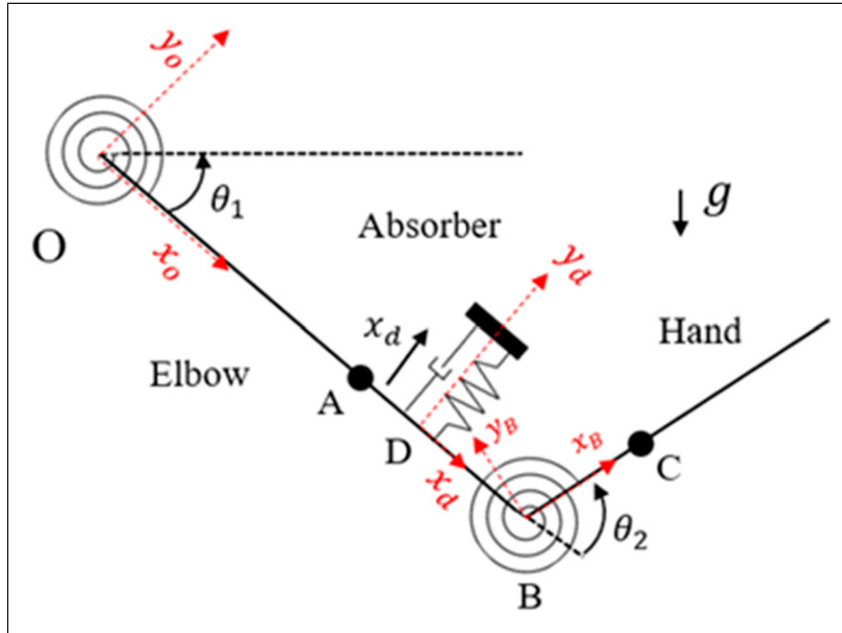


**Figure 3.** The human forearm and hand model.

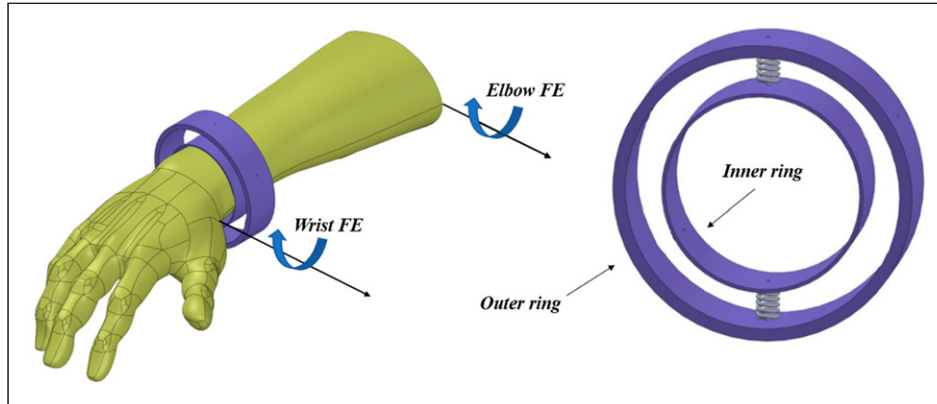


**Figure 4.** A real-world representation of the developed absorber.

$$\frac{d}{dt} \frac{\partial(T - U)}{\partial \dot{q}^J} - \frac{\partial(T - U)}{\partial q^J} = Q_J - \frac{\partial \mathfrak{R}}{\partial \dot{q}^J}, \mathfrak{R} = \sum_J \frac{1}{2} c_J \dot{q}^J \quad (31)$$

$$\begin{aligned} T = & \frac{I_{C1}}{2} (\dot{\theta}_1)^2 + \frac{I_{C2}}{2} (\dot{\theta}_1 + \dot{\theta}_2)^2 + \frac{m_1}{2} (l_{c1} \dot{\theta}_1)^2 \\ & + \frac{m_d}{2} \left( \left( \dot{\theta}_1 \sqrt{x_d^2 + l_d^2} \right)^2 + \dot{x}_d^2 + 2\dot{\theta}_1 \dot{x}_d l_d \right) \\ & + \frac{m_2}{2} ((l_1 \times \dot{\theta}_1)^2 + (l_{c2} (\dot{\theta}_2 + \dot{\theta}_1))^2 \\ & + 2l_1 l_{c2} \dot{\theta}_1 (\dot{\theta}_2 + \dot{\theta}_1) \cos(\theta_2)) \end{aligned} \quad (32)$$

where  $I_{C1}$  and  $I_{C2}$  are the rotational moments of inertia for the forearm and hand around their centers of masses. By

taking point O to have zero potential, the potential energy of the system is calculated as well:

$$\begin{aligned} U = & m_1 g l_{c1} \times \sin(\theta_1) + \frac{1}{2} k_{t1} \theta_1^2 + \frac{1}{2} k_d x_d^2 + \frac{1}{2} k_{t2} \theta_2^2 \\ & + m_d g (l_d \times \sin(\theta_1) + x_d \cos(\theta_1)) + m_2 (l_1 \sin(\theta_1) \\ & + l_{c2} \sin(\theta_1 + \theta_2)) \end{aligned} \quad (33)$$

where  $k_{t1}$  and  $k_{t2}$  are the passive rotational stiffness of the elbow and wrist joints, respectively. Also  $k_d$  is the effective

stiffness of the viscous absorber. For the Rayleigh's dissipation factor, we have the following:

$$\Re = \frac{1}{2}c_1\dot{\theta}_1^2 + \frac{1}{2}c_d\dot{x}_d^2 + \frac{1}{2}c_2\dot{\theta}_2^2 \quad (34)$$

Exerted torques to joints are summation of voluntary (postural) and involuntary (tremor induced) torques. The joint torques can be determined as follows:

$$T_1 = g(m_1 l_{c1} \cos(\theta_1) + m_2(l_1 \cos(\theta_1) + m_d(l_d \cos(\theta_1) + x_d \sin(\theta_1))) + T_{tremor1} \quad (35)$$

$$T_2 = l_{c2}g m_2 \cos(\theta_1 + \theta_2) + T_{tremor2} \quad (36)$$

where  $T_{tremor}$  indicate tremor-induced torques and the 1 and 2 subscripts refer to the elbow and wrist joints, respectively. To tune the absorbers, we have taken the tremors to be a sinusoidal torque with unit amplitude (Ture Savadkoohi et al., 2021) and varying frequency. Using the principle of virtual work, generalized force and torques can be calculated:

$$Q_1 = T_1 + T_2 + \mathcal{F}_{SMA}l_{c1} \quad (37)$$

$$Q_2 = T_2 \quad (38)$$

$$Q_3 = \mathcal{F}_{SMA} \quad (39)$$

where  $Q_1$ ,  $Q_2$ , and  $Q_3$  are generalized torques and forces for the coordinates  $\theta_1$ ,  $\theta_2$ , and  $x_d$ .  $\mathcal{F}_{SMA}$  refers to the sum of exerted force from SMA springs to patient's forearm. It is important to note that we have represented SMA and classic absorbers in one formulation for the purposes of brevity. We can easily get the response of viscous and SMA absorber by taking  $\mathcal{F}_{SMA} = 0$  and  $c_d = k_d = 0$ , respectively. By placing (32)–(39) in (31), the governing differential equations are derived, (40)–(42). This ode system is non-stiff and is solved using a custom implementation of MATLAB's ode15s module.

$$\begin{aligned} T_1 + T_2 + \mathcal{F}_{SMA} - c_1\dot{\theta}_1 = \\ gl_{c1}m_1 \cos(\theta_1) + gl_1m_2 \cos(\theta_1) + gl_dm_d \cos(\theta_1) \\ + gl_{c2}m_2 \cos(\theta_1 + \theta_2) + k_{t1}\theta_1 - 2l_1l_{c2}m_2 \sin(\theta_2)\dot{\theta}_1\dot{\theta}_2 \\ - 2l_1l_{c2}m_2 \sin(\theta_2)\dot{\theta}_2^2 - m_d x_d(g \sin(\theta_1) - 2\dot{\theta}_1\dot{x}_d) \\ + I_{C1}\theta_1 + I_{C2}\ddot{\theta}_1 \\ + l_{c1}^2m_1\ddot{\theta}_1 + l_1^2m_2\ddot{\theta}_1 + l_{c2}^2m_2\ddot{\theta}_1 \\ + l_d^2m_d\ddot{\theta}_1 + x_d^2m_d\ddot{\theta}_1 + I_{C2}\ddot{\theta}_2 \\ + l_{c2}^2m_2\ddot{\theta}_2 + l_1l_{c2}m_2 \cos(\theta_2)\ddot{\theta}_2 + I_d m_d \ddot{x}_d \end{aligned} \quad (40)$$

$$\begin{aligned} T_2 - c_2\dot{\theta}_2 = \\ gl_{c2}m_2 \cos(\theta_1 + \theta_2) + k_{t2}\theta_2 + l_1l_{c2}m_2 \sin(\theta_2)\dot{\theta}_1^2 + I_{C2}\ddot{\theta}_1 \\ + l_1l_{c2}m_2 \cos(\theta_2)\dot{\theta}_1 + I_{C2}\theta_2 + l_{c2}^2m_2\theta_2 \end{aligned} \quad (41)$$

$$\mathcal{F}_{SMA} - c_d\dot{x}_d = x_d(k_d - m_d\dot{\theta}_1^2) + m_d(g \cos(\theta_1) + l_d\ddot{\theta}_1 + \ddot{x}_d) \quad (42)$$

The obtained ODE system is validated with ADAMS. Also, all the values of the structural variables in the model are adopted from experiments conducted by de Leva (1996). This is except for the passive stiffness and damping of the joints. Only a few researches were conducted on quantifying the passive stiffness and damping of human upper joints, and the existing researches presented very different results. This is due to the fact that the passive stiffness and damping of the joints (I) depend on the amount of force exerted on the joint, (II) depend on the thickness of tendons, which varies from patient to patient (Roy et al., 2011), and (III) are not constant as the joint deviates in different directions (Formica et al., 2012). Using the formulation introduced by Formica et al. (2012),  $k_{t1}$  is determined to be 1.05 Nm/rad and 1.3125 Nm/rad for flexion and extension of the wrist, respectively. Also, using a linear regression of experiments conducted by Endo et al. (2009),  $k_{t2}$  is found to be 2.19 Nm/rad and 2.62 Nm/rad for flexion and extension of the elbow joint.  $c_1$  and  $c_2$  also were determined by the works of Popescu et al. (2003) and Milner and Cloutier (1998). Here, we take passive damping of wrist and elbow (i.e.,  $c_1$  and  $c_2$ ) to be 0.104 Nms/rad and 0.088 Nms/rad for the elbow's flexion and extension, and 0.017 Nms/rad for both flexion and extension of the wrist.

## 4. Optimization

Despite the simplicity of developing passive absorbers for vibration mitigation, these devices should be tuned for efficient performance. In this work, no linearization was used, which called for a numerical approach in optimization. Numerical methods such as ant colony (Viana et al., 2008), differential evolution (Lu et al., 2018a), and genetic algorithm (Mohebbi and Joghataie, 2011) were used in the literature for absorber optimization. We tuned both SMA and viscous absorbers using genetic algorithm (GA). The optimization parameters were  $m_d$ ,  $l_d$ ,  $k_d$  and  $c_d$  for the viscous absorber and  $m_d$ ,  $l_d$ ,  $d$ ,  $D$ ,  $N$ ,  $l_0$  and the prestrain for the SMA absorber. The idea behind prestraining SMA springs is to facilitate their phase transformation. This point is also noted by Thomson et al. (1995). They observed that the effective damping of SMA wires increased when they were prestrained properly.

The cost function was defined as the area under the wrist frequency response for both the SMA and the viscous absorber. The cost function formulation is presented in (45) in which the integration range is defined by the tremor frequency range for PD and ET (i.e., 4–12 Hz).

$$cost_{Area} = \int_{f_{min}}^{f_{max}} abs(\theta_2^{steady\ state}) df \quad (43)$$

The optimization process was run twice for each absorber to assure that the optimization has converged to the optimal point. Figure 5(a) and (b) depicts the optimization process for the viscous absorber. As seen in Figure 5(a), the cost decreases as  $l_d$  increases which can be explained by the increase in absorber's exerted torque to elbow joint. By looking at Figure 5(b), we can see that the optimization cost decreases as the absorber mass increases which comes with the cost of lower user experience. We took the upper bound of absorber mas to be 0.16 kg to have the least interference with patients' daily life, while preserving absorber effectiveness. But proportional relation of  $l_d$  and  $m_d$  with cost can't be generalized to  $k_d$  and  $c_d$ , where we can see that the amounts converge to  $378.99 \frac{N}{m}$  and  $16.437 \frac{Ns}{m}$ , respectively.

Seven parameters were used in SMA absorber optimization. Although seven parameters cannot be analyzed in 3-dimensional scatter plots, we use the spring's stiffness when there is no phase transformation in it to draw conclusions on the optimization process and spring parameters in a general basis. The spring stiffness is calculated in (44). The SMA

absorber optimization was conducted with a minimum spring stiffness (when it's full-austenite) of 200 N/m to preserve the spring construction feasibility.

As shown in Figure 6, as the absorber mass increases, the population cost decreases which was observed in the viscous absorber as well. Another point to note is the quick convergence to the spring stiffness limit. The lower the spring stiffness or the higher the absorber mass, there is more chance of phase transformation in the spring cross-section due to high stress, resulting in developing hysteresis loops and dissipating energy.

$$k_{Spring} = \frac{G_{Austenite} d^4}{8ND^3} \quad (44)$$

## 5. Results and discussion

### 5.1. Harmonic excitation

Both the SMA and viscous absorbers were tuned by assuming a harmonic excitation as the source of the joint tremor. The parameters of the tuned absorbers are stated in Table 1. Each of the SMA and the viscous absorbers have reduced the amplitude and kinetic energy of the undamped system to different extents. Additionally, the optimized absorbers are excited with an amplitude twice the size of what they were optimized for, to analyze their durability against unexpected forces. In the following diagrams, the acquired responses for Undamped system, and SMA and viscous absorbers under unit and 2 Nm/rad amplitude excitations are regarded to as

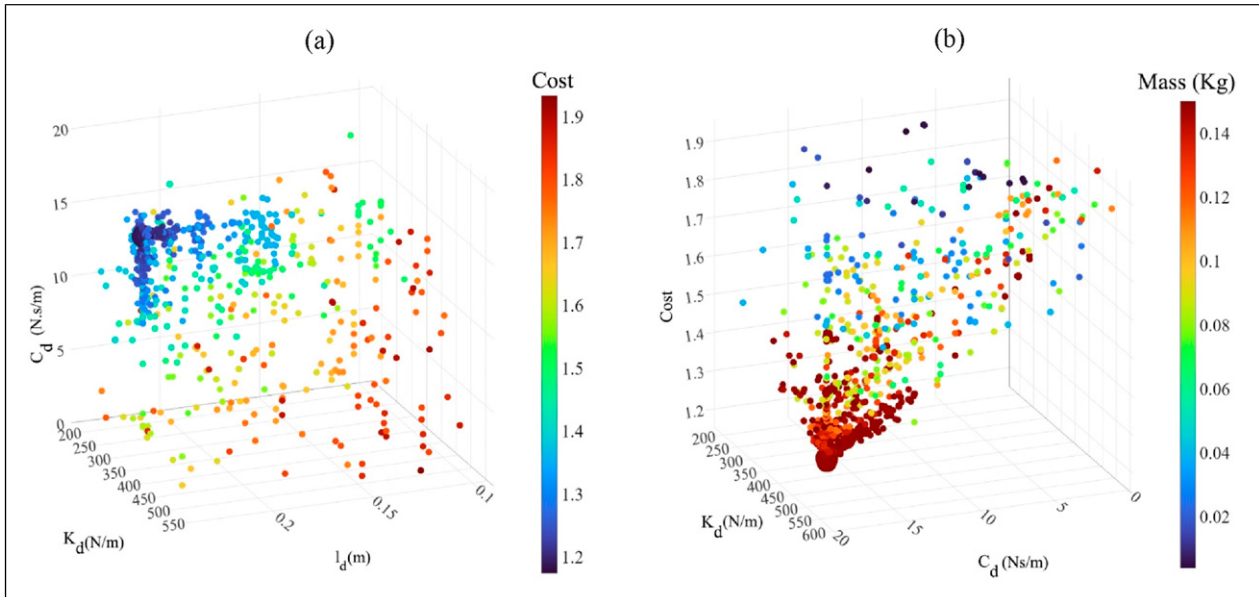


**Figure 5.** GA results for viscous absorber optimization. (a) plots  $c_d$ ,  $k_d$ ,  $l_d$  and cost while, (b) plots cost,  $k_d$ ,  $c_d$  and  $m_d$  of the generated population through the end of the optimization. The larger the point size, the more members of the generation was found around that point (with a logarithmic basis).

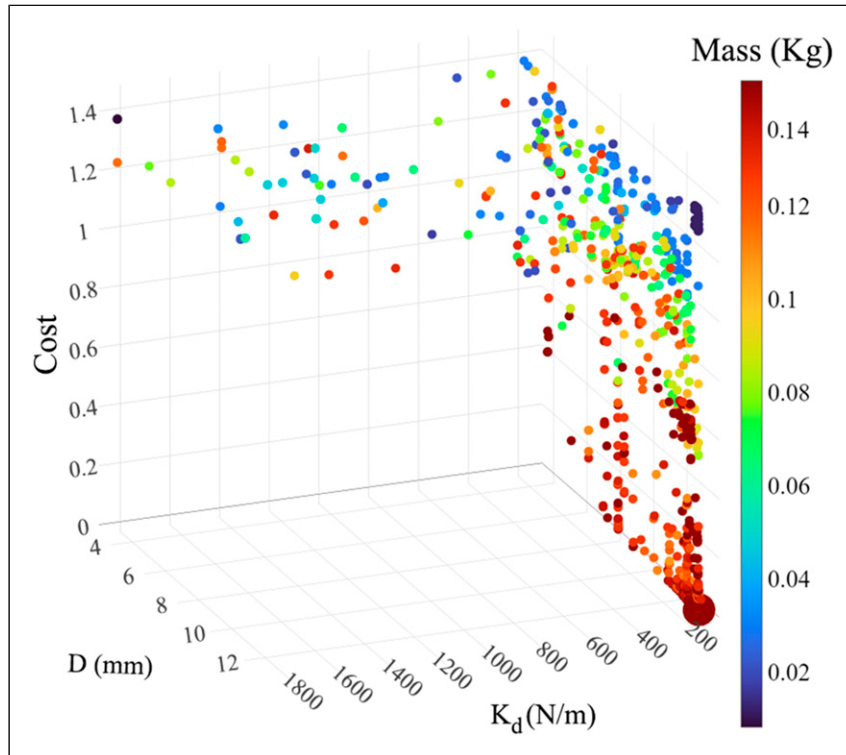


**Figure 6.** GA optimization populations of SMA absorber in 4 dimensions: spring's calculated stiffness ( $K$ ), absorber mass ( $m_d$ ), coil diameters ( $D$ ), and the cost. The larger the point size, the more members of the generation was found around that point (with a logarithmic basis).

**Table I.** Optimization parameters of viscous and SMA absorbers, their search ranges, and final results for the optimization.

Optimized value	Search range	Parameter	
0.1598 kg	[0, 0.16]	$m_d$ (kg)	Viscous
0.1697 m	[0, 0.24]	$l_d$ (m)	
378.9912 N/m	[0.5, 500]	$k_d$ (N/m)	
16.4374 Ns/m	[0.5, 20]	$c_d$ (Ns/m)	
0.1599 kg	[0, 0.16]	$m_d$ (kg)	SMA
0.2336 m	[0, 0.24]	$l_d$ (m)	
1.0009 mm	[0.2, 1.5]	$d$ (mm)	
13.522 mm	[4, 15]	$D$ (mm)	
8.0053	[3, 15]	$N$	
16.7856 mm	[5, 20]	$l_0$ (mm)	
18.8862%	[0, 100]	prestrain(%)	

Undamped-I, SMA-I, Viscous-I, Undamped-II, SMA-II and Viscous-II. To compare the absorbers' performances, the reduction at every frequency is calculated by (45).

$$\text{Reduction} = \frac{\theta_{\text{Undamped}} - \theta_{\text{Damped}}}{T_{\text{Undamped}}} \times 100 \quad (45)$$

As can be seen in Figure 7, SMA-I can achieve maximum amplitude reduction of 91.5% and 90.2% for the elbow and

wrist, while for Viscous-I, these values are 84.7% and 89.4%, which means that SMA-I performs better in reducing resonance amplitude. Using SMA or viscous absorber results in roughly the same amount of maximum amplitude reduction of the wrist. However, as shown in Figure 7(a), Viscous-I worsens the maximum tremor amplitude at the elbow, while SMA-I causes a 23.4% reduction. Furthermore, because the absorbers are optimized for a unit amplitude excitation, a detuning takes place as it is seen on Figure 7(a) and (b). The detuned SMA absorber (SMA-II) performs worse than Viscous-II in reducing the maximum tremor amplitude in both joints. And, for the resonance frequency, while SMA-II performs better for the elbow, there is negligible outperformance in using SMA-II instead of Viscous-II for the wrist.

A comparative analysis based on energy can also be conducted to further analyze the absorbers. Figure 8(a) represents the kinetic energy of the entire model at various excitation frequencies. Both SMA-I and Viscous-I absorbers have a considerable (and roughly the same) effect on decreasing the resonance kinetic energy of the undamped system. Also, referring to this figure, it can be inferred that SMA-I can cause a 78% reduction in the maximum kinetic energy of the system. In contrast, this measure for Viscous-I is only 27%, 49% less than that of SMA-I's. Regarding SMA-II and Viscous-II, both absorbers

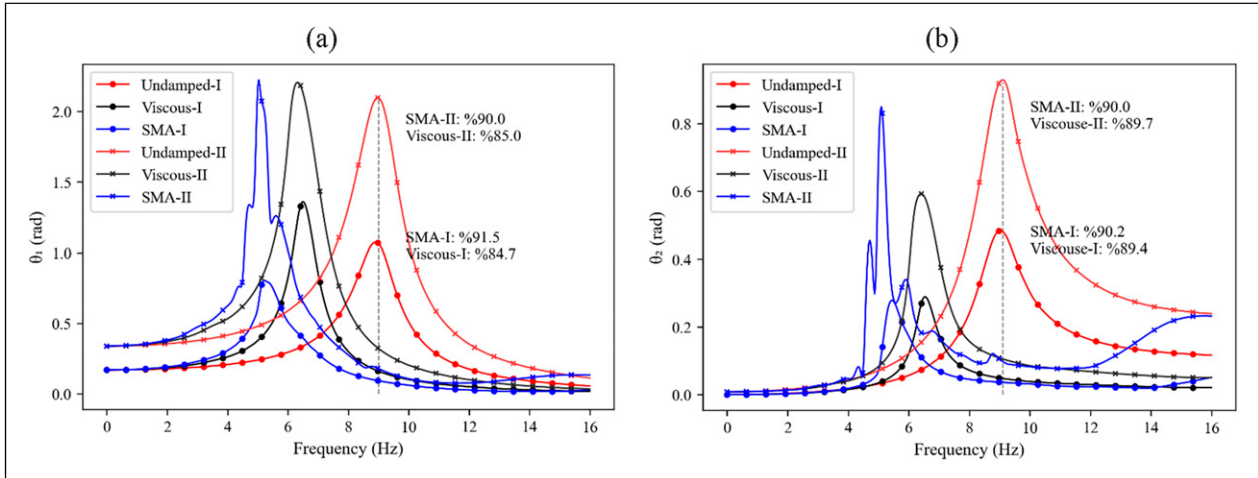


**Figure 7.** The final results of the optimization. The frequency response at (a) elbow and (b) wrist. The blue, black, and red lines represent the results of the SMA absorber, viscous absorber, and undamped system. The frequency responses for unit and 2 Nm/rad excitations are decorated with circle and cross markers.

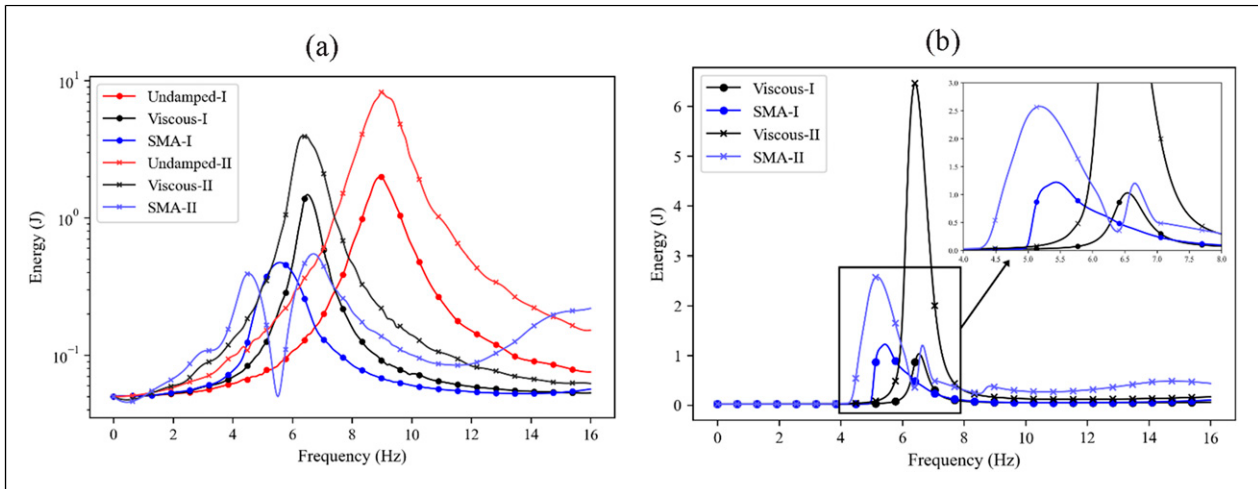


**Figure 8.** (a) The kinetic energy of the entire system and (b) the dissipated energy by the absorbers in each steady-state cycle. The blue, black, and red lines represent the results of the SMA absorber, viscous absorber, and undamped system. The frequency responses for unit and 2 Nm/rad excitations are decorated with circle and cross markers.

decrease resonance kinetic energy of the system to more than 99%, but still SMA-II performs better than Viscous-II.

Figure 8(b) shows the dissipated energy by absorbers which is acquired by computing the area inside the force-displacement curve of the absorber in each steady-state cycle. As it can be seen only in the frequency range from 6.3 Hz to 7.1 Hz, Viscous-I has better absorbing capability than the SMA-I. Also, referring to Figure 8(b), it is seen that Viscous-II is capable of absorbing more energy in 6 Hz to 8 Hz and, unlike the optimized systems, Viscous-II has a much higher maximum damped energy.

The hysteresis loops generated by absorbers under unit amplitude loading are depicted in Figure 9. The solid blue and red lines in each sub-plot refer to the first and second SMA spring's displacement versus its reaction force, while black

curves represent the said relation for the viscous absorber. The area inside the curves belonging to each absorber is equal to the dissipated energy in each steady-state cycle. The energy dissipation in SMA increases sharply from 5 Hz to 5.6 Hz. However, this is due to the increase in steady-state displacement amplitude of the absorber mass as the system approaches its resonance frequency. This fact is also stated by Lu et al. (2018b). They note that the dissipative capacity of NESs is amplitude-dependent, while vibration frequency has no direct impact on it. For easier phase transformation of SMA springs, they have been prestrained. This is the reason for the asymmetric hysteresis loops in SMA springs in Figure 9, while the hysteresis loops for the viscous absorber are symmetric. Referring to Figure 9, we can see that the

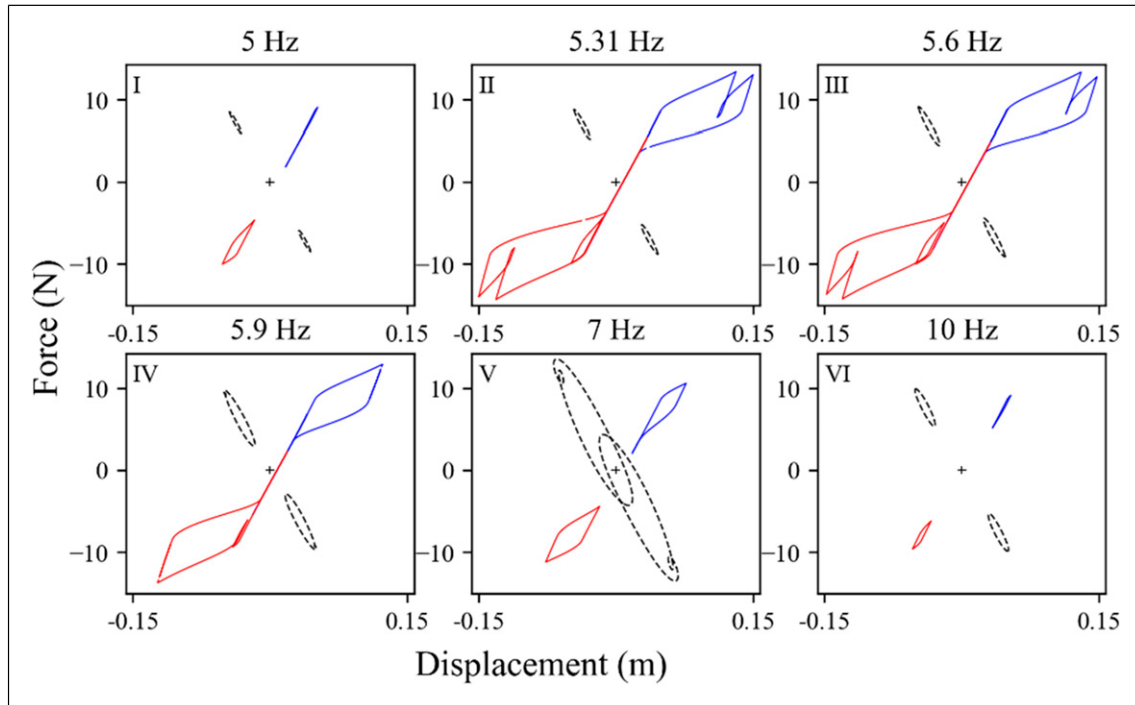


**Figure 9.** The force–displacement hysteresis loops generated by absorbers at different frequencies with unit tremor amplitude. The x and y axis of each sub-plot reflect the displacement made by absorber (m) and the force exerted by it (N). Solid blue and red lines refer to the upper and lower SMA springs in the SMA absorber, respectively. Dashed black lines represent hysteresis loops for viscous absorbers which act the same in a complete cycle.

SMA-I reaches its peak absorption capability at 5.6 Hz and then gradually, the damped energy decreases. With the same perspective, we can see that at 7 Hz, Viscous-I acts considerably better than the SMA absorber in absorbing vibration energy. However, as the vibration frequency increases, these absorbers have roughly the same absorption capacity.

It is important to note that all patients cannot use the presented absorbers. Referring to Figure 7, it can be seen at some frequencies, the absorbers can worsen the tremor, and the patient is better off not using the absorber (SMA or viscous). Let us call the frequency at which the absorber starts to mitigate the tremor, the effectiveness frequency (EF). The EF for the Viscous-I is 7.3 Hz and 7.8 Hz for the elbow and wrist, while SMA-I's EF is 6.8 Hz and 6.7 Hz for elbow and wrist tremor frequencies. This fact means that SMA-I can perform in a wider range of frequencies and benefit a larger group of patients.

## 5.2. Random excitation

Harmonic excitations provide important information about system's structural parameters and natural frequencies. However, in order to more realistically evaluate the absorbers, real tremor data were used as excitation as well. The dataset contained inertial measurement unit (IMU) data collected from 34 individuals, 15 of whom had Parkinson's (Russell et al., 2023). The IMUs recorded the acceleration at a 0.02 s sampling rate while patients made a toast. The

power spectral density (PSD) of the joint's amplitude was calculated using the Welch–Bartlett method (Welch, 1967) with 512 Hamming windows and a 50% overlap.

The PSD evaluation is generalized for all patients, and the results are depicted in Figures 10 and 11. The points at which using absorber results in an increase in the amplitude PSD are colored in red. It can be seen that for the elbow (Figure 10), both SMA and viscous absorbers exhibit poor performance at 0.4 Hz, 1.3 Hz, and 1.5 Hz, and for the frequencies larger than 1.5 Hz, both absorbers are able to reduce the tremor power. For the wrist (Figure 11), the SMA absorber causes an increase in tremor power at 0.5 Hz and 2 Hz, whereas the viscous absorber causes power reduction at the frequency range of 0–25 Hz.

It is known that voluntary motion has frequency spectra below 2 Hz, while involuntary motions have frequency spectra higher than 2 Hz (Herrnstadt et al., 2019). Thus, the ideal absorber performance would be minimal PSD reduction in the 0–2 Hz range while maximal reduction for frequencies larger than 2 Hz. Figure 12 represents the average amplitude power reduction for all patients. Referring to this chart, it can be noted that the viscous absorber performs better in not interfering with voluntary motions. However, the SMA absorber reduces tremor power up to 92% in the frequency range of 3–25 Hz, which is significantly better than an average 55% reduction achieved by the viscous absorber. Also, it is noteworthy that as the spectra frequency approaches 25 Hz, the viscous absorber's power reduction catches up with SMA's.

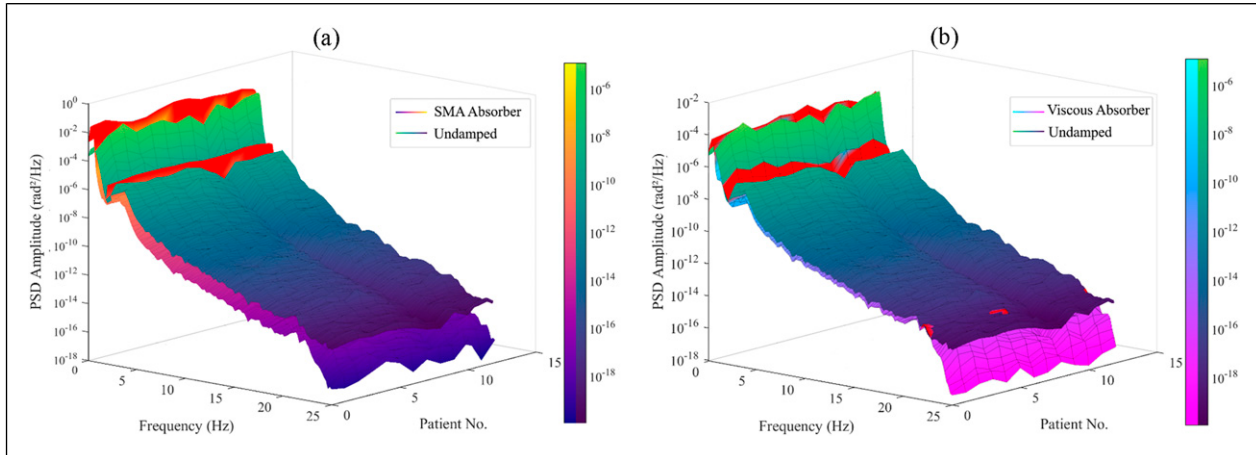


**Figure 10.** The comparison between elbow amplitude PSD for all patients without using any absorbers versus using (a) the SMA absorber and (b) the viscous absorber.

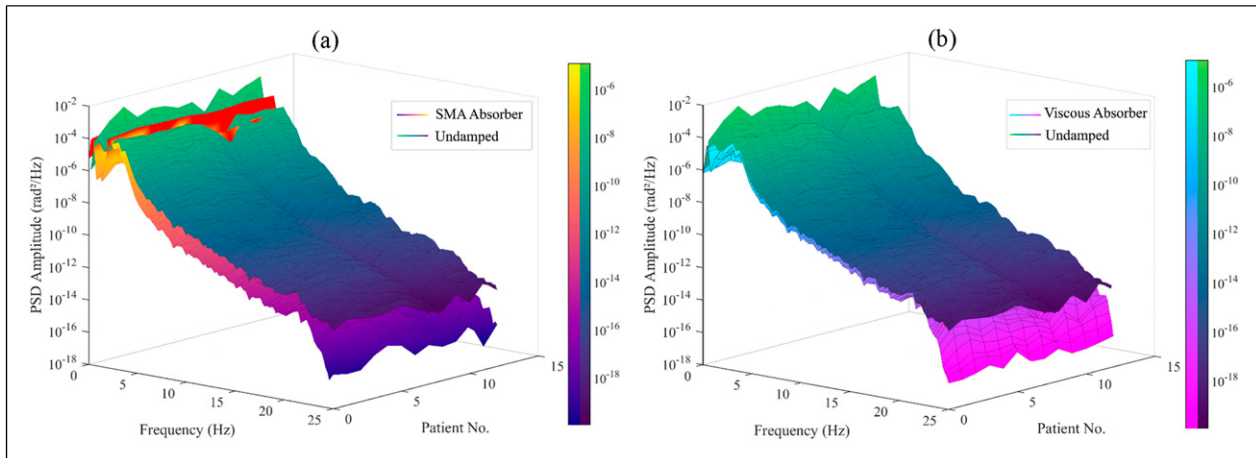


**Figure 11.** The comparison between wrist amplitude PSD for all patients without using any absorbers versus using (a) the SMA absorber and (b) the viscous absorber.

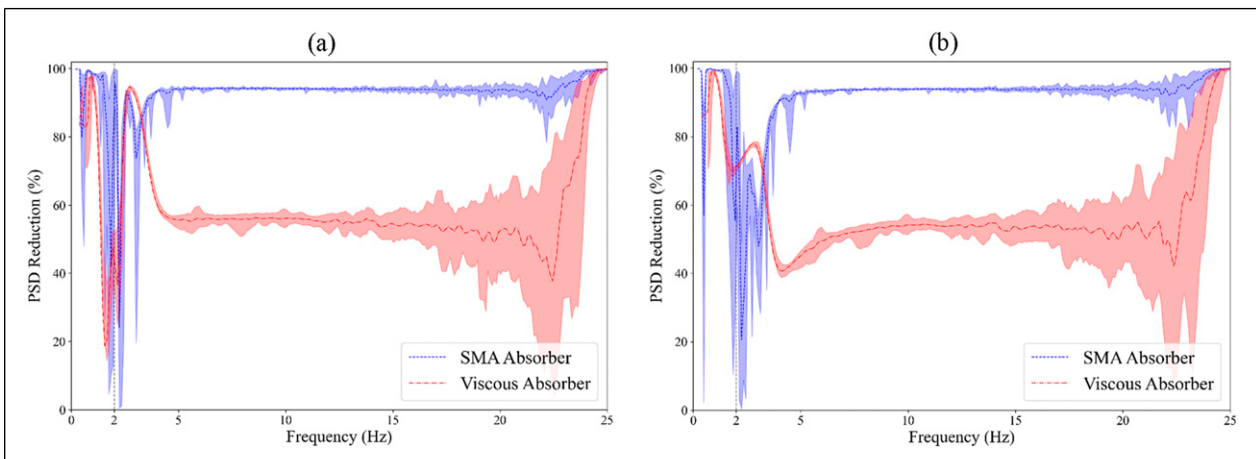


**Figure 12.** PSD percentage reduction in (a) elbow and (b) wrist for all patients. Blue and red lines refer to the average amplitude reduction in all of the patients using SMA and viscous absorbers, respectively. The blue and red areas indicate maximum and minimum amplitude reduction at a certain frequency across all patients.

One of the notable advantages of using SMA springs instead of a classic spring–damper pair is the reduction in the moving parts of the absorber while enhancing its performance, which is an extremely difficult task (Elias and Matsagar, 2017).

It is important to note that all of the simulation results for the SMA absorber are obtained with the assumption of the springs being 100% austenite at ambient temperature. With the current material properties, if the ambient temperature is less than 290 K, some of the austenite in the spring's microstructure will transform to martensite. This will lead to smaller hysteresis loops and lower performance. It is, therefore, necessary to change the spring material if the SMA absorber is to be used at lower temperatures.

## 6. Conclusion

In the current work, a passive energy sink is developed to reduce wrist and elbow tremors for patients who have Parkinson's disease or natural tremors. The proposed device uses a single shape memory alloy spring instead of a spring–damper pair, which halves the moving parts of the absorber. The simulations were conducted with both harmonic excitations and real-world tremor data. The results indicated that the SMA absorber did a better job at reducing the resonance amplitude than the viscous absorber. Also, when under random excitations, the SMA absorber reduced the tremor power significantly more than the viscous absorber in the range of 3–25 Hz. In contrast, the viscous absorber did a better job at not interfering with the patient's voluntary movements.

Despite the promising results of the simulations of the proposed SMA absorber for reducing tremors, future studies may be able to achieve more accurate results if the DOFs of the hand model are increased to account for shoulder FE or wrist's radial–ulnar and pronation–supination.

## Acknowledgments

We would like to thank Dr. Arash Bahrami, Mr. Ali Khastavan, and Mr. Hossein Sahbafor for their intellectual help and valuable insights in the process of completing this work.

## Declaration of conflicting interests

The author(s) declared no potential conflicts of interest with respect to the research, authorship, and/or publication of this article.

## Funding

The author(s) received no financial support for the research, authorship, and/or publication of this article.

## ORCID iD

Abbas Jafarpour Mahalleh  <https://orcid.org/0009-0002-9553-0727>

## Data availability statement

The simulation files are shared in the main author's public GitHub repository located at: <https://github.com/amirabbasja>.

## Supplemental Material

Supplemental material for this article is available online.

## References

- Aguiar RAA, Savi MA and Pacheco PMCL (2010) Experimental and numerical investigations of shape memory alloy helical springs. *Smart Materials and Structures* 19(2): 025008.
- Alexander NA and Schilder F (2009) Exploring the performance of a nonlinear tuned mass damper. *Journal of Sound and Vibration* 319(1–2): 445–462.
- Brinson LC (1993) One-dimensional constitutive behavior of shape memory alloys: thermomechanical derivation with non-constant material functions and redefined martensite internal variable. *Journal of Intelligent Material Systems and Structures* 4(2): 229–242.
- Brinson LC and Huang MS (1996) Simplifications and comparisons of shape memory alloy constitutive models. *Journal of Intelligent Material Systems and Structures* 7(1): 108–114.
- Budynas R and Nisbett K (2014) *Shigley's Mechanical Engineering Design*. New York, NY: McGraw-Hill Higher Education - VST E+p.
- Das S, Chakraborty S, Chen Y, et al. (2021) Robust design optimization for SMA based nonlinear energy sink with negative stiffness and friction. *Soil Dynamics and Earthquake Engineering* 140: 106466.
- Davidson AD and Charles SK (2017) Fundamental principles of tremor propagation in the upper limb. *Annals of Biomedical Engineering* 45(4): 1133–1147.
- de Leva P (1996) Adjustments to Zatsiorsky-Seluyanov's segment inertia parameters. *Journal of Biomechanics* 29(September): 1223–1230.
- Deuschl G, Bain P and Brin M (1998) Consensus statement of the movement disorder society on tremor. Ad hoc scientific committee. *Movement Disorders: Official Journal of the Movement Disorder Society* 13(Suppl 3): 2–23.
- Ding H and Chen LQ (2020) Designs, analysis, and applications of nonlinear energy sinks. *Nonlinear Dynamics* 100: 3061–3107. DOI: [10.1007/s11071-020-05724-1](https://doi.org/10.1007/s11071-020-05724-1).
- Elias S and Matsagar V (2017) Research developments in vibration control of structures using passive tuned mass dampers. *Annual Reviews in Control* 44: 129–156.
- Endo T, Okuno R, Yokoe M, Akazawa K and Sakoda S (2009) A novel method for systematic analysis of rigidity in Parkinson's disease. 24(15): 2218–2224.
- Enemark S, Savi MA and Santos IF (2014) Nonlinear dynamics of a pseudoelastic shape memory alloy system - theory and experiment. *Smart Materials and Structures* 23(8): 085018.
- Formica D, Charles SK, Zollo L, et al. (2012) The passive stiffness of the wrist and forearm. *Journal of Neurophysiology* 108: 1158–1166.
- Fromme NP, Camenzind M, Riener R, et al. (2020) Design of a lightweight passive orthosis for tremor suppression. *Journal of NeuroEngineering and Rehabilitation* 17: 1–15.
- Gebai S, Hammoud M, Hallal A, et al. (2018) Structural control and biomechanical tremor suppression: comparison between

- different types of passive absorber. *Journal of Vibration and Control* 24(12): 2576–2590.
- Gourdon E and Lamarque CH (2006) Nonlinear energy sink with uncertain parameters. *Journal of Computational and Nonlinear Dynamics* 1(3): 187–195.
- Heidari B, Kadkhodaei M, Barati M, et al. (2016) Fabrication and modeling of shape memory alloy springs. *Smart Materials and Structures* 25(12): 125003.
- Herrnstadt G, McKeown MJ and Menon C (2019) Controlling a motorized orthosis to follow elbow volitional movement: tests with individuals with pathological tremor. *Journal of Neuro Engineering and Rehabilitation* 16(1): 23.
- Hosseini SM, Kalhor H and Al-Jumaily A (2020) Active vibration control in human forearm model using paired piezoelectric sensor and actuator. *Journal of Vibration and Control* 27(19–20): 2231–2242.
- Huang B, Lv H and Song Y (2018) Numerical simulation and experimental study of a simplified force-displacement relationship in superelastic sma helical springs. *Sensors* 19(1): 50.
- Kodek T and Munih M (2003) An analysis of static and dynamic joint torques in elbow flexion-extension movements. *Simulation Modelling Practice and Theory* 11(3–4): 297–311.
- Liang C and Rogers C (1991) The multi-dimensional constitutive relations of shape memory alloys. In: 32nd structures, structural dynamics, and materials conference, Baltimore, MD, 8–10 April 1991, 429–443. DOI: [10.2514/6.1991-1165](https://doi.org/10.2514/6.1991-1165).
- Louis ED (1997) Tremor disorders: identification and treatment. *Medical Update for Psychiatrists* 2(6): 172–176.
- Lu Z and Huang Z (2021) Analytical and experimental studies on particle damper used for tremor suppression. *Journal of Vibration and Control* 27(23–24): 2887–2897.
- Lu Z, Lu X, Lu W, et al. (2012) Experimental studies of the effects of buffered particle dampers attached to a multi-degree-of-freedom system under dynamic loads. *Journal of Sound and Vibration* 331(9): 2007–2022.
- Lu Z, Yang Y, Lu X, et al. (2017) Preliminary study on the damping effect of a lateral damping buffer under a debris flow load. *Applied Sciences* 7(2): 201.
- Lu Z, Li K, Ouyang Y, et al. (2018a) Performance-based optimal design of tuned impact damper for seismically excited nonlinear building. *Engineering Structures* 160: 314–327.
- Lu Z, Wang Z, Zhou Y, et al. (2018b) Nonlinear dissipative devices in structural vibration control: a review. *Journal of Sound and Vibration* 28: 18–49.
- Lu Z, Rong K, Tian L, et al. (2022) Studies on the damping mechanism of shape memory alloy-spring tuned vibration absorber attached to a multi-degree-of-freedom structure. *Journal of Vibration and Control* 28(19–20): 2666–2677.
- Milner TE and Cloutier C (1998) Damping of the wrist joint during voluntary movement. *Experimental Brain Research* 122(3): 309–317.
- Mohammad Hashemi Y, Kadkhodaei M and Mohammadzadeh MR (2019) Fatigue analysis of shape memory alloy helical springs. *International Journal of Mechanical Sciences* 161–162: 105059.
- Mohd Jani J, Leary M, Subic A, et al. (2014) *A Review of Shape Memory Alloy Research, Applications and Opportunities*. Amsterdam, the Netherlands: Elsevier Ltd, 1078–1113.
- Mohebbi M and Joghataie A (2011) Designing optimal tuned mass dampers for nonlinear frames by distributed genetic algorithms. *The Structural Design of Tall and Special Buildings* 24: 421–439.
- Park Y-h, Kwon S-c, Koo K-r, et al. (2021) High damping passive launch vibration isolation system using superelastic SMA with multilayered viscous lamina. *Aerospace* 8(8): 201.
- Popescu F, Hidler JM and Rymer WZ (2003) Elbow impedance during goal-directed movements. *Experimental Brain Research* 152(1): 17–28.
- Rahnavard M, Hashemi M, Farahmand F, et al. (2014) Designing a hand rest tremor dynamic vibration absorber using H2 optimization method. *Journal of Mechanical Science and Technology* 28(5): 1609–1614.
- Roy A, Krebs HI, Bever CT, et al. (2011) Measurement of passive ankle stiffness in subjects with chronic hemiparesis using a novel ankle robot. *Journal of Neurophysiology* 105(5): 2132–2149.
- Ruonala V, Meigal A, Rissanen SM, et al. (2014) EMG signal morphology and kinematic parameters in essential tremor and Parkinson's disease patients. *Journal of Electromyography and Kinesiology: Official Journal of the International Society of Electrophysiological Kinesiology* 24(2): 300–306.
- Russell J, Inches J, Carroll C, et al. (2023) A five-sensor IMU-based Parkinson's disease patient and control dataset including three activities of daily living [dataset]. *Dryad*. Available at: <https://doi.org/10.5061/dryad.fbg79cp1d>.
- Shaw J-s and Wang C-a (2019) Design and control of adaptive vibration absorber for multimode structure. *Journal of Intelligent Material Systems and Structures* 30: 1043–1052.
- Stoker TB, Torsney KM and Barker RA (2018) Emerging treatment approaches for Parkinson's disease. *Frontiers in Neuroscience* 12: 1–10.
- Taghipour J and Dardel M (2015) Steady state dynamics and robustness of a harmonically excited essentially nonlinear oscillator coupled with a two-DOF nonlinear energy sink. *Mechanical Systems and Signal Processing* 62–63: 164–182.
- Thomson P, Balas GJ and Leo PH (1995) The use of shape memory alloys for passive structural damping. *Smart Materials and Structures* 4(1): 36–41.
- Ture Savadkoohi A, Lamarque CH and Goossaert C (2021) Nonlinear passive tremor control of human arm. *Mechanical Systems and Signal Processing* 146: 107041.
- Viana FAC, Kotinda GI, Rade DA, et al. (2008) Tuning dynamic vibration absorbers by using ant colony optimization. *Computers & Structures* 86(13–14): 1539–1549.
- Wang T, Tian R, Yang X, et al. (2021) A novel dynamic absorber with variable frequency and damping. *Shock and Vibration* 2021(1): 10.
- Welch PD (1967) The use of fast fourier transform for the estimation of power spectra: a method based on time averaging over short, modified periodograms. *IEEE Transactions on Audio and Electroacoustics* 15(2): 70–73.
- Whal AM (1963) *Mechanical Springs*. New York, NY: McGraw-Hill Book Company.
- Zubair M, Suthar B and Jung S (2022) Design and analysis of flexure mechanisms for human hand tremor compensation. *IEEE Access* 10: 36006–36017.